This manuscript is a non-peer reviewed preprint submitted to EarthArXiv.
It has been submitted to Geophysical Journal International (GJI) for peer review.

Predictive modeling of seismic wave fields: Learning the transfer function using encoder-decoder networks

Jana Klinge [1], Sven Schippkus[1], Jan Walda[1,2], Celine Hadziioannou[1], Dirk Gajewski [1] *

[1] Institute of Geophysics, Centre for Earth System Research and Sustainability (CEN), Universität Hamburg, Hamburg, Germany
[2] Currently: Emetriq GmbH, Hamburg, Germany
* Correspondence: jana.klinge@uni-hamburg.de

Abstract:

Wouldn't it be beneficial if we could predict the time series at a seismic station even if the station no longer exists? In geophysical data analysis, this capability would enhance our ability to study and monitor seismic events and seismic noise, particularly in regions with incomplete station coverage or where stations are temporarily offline. This study introduces a novel adaption of encoder-decoder networks from the subfield of Deep Learning, modified to predict the development of seismic wave fields between two seismic stations. Using one-dimensional time series measurements, our algorithm aims to learn and predict signal transformations between the two stations by approximating the transfer function. Initially, we evaluate this proof of concept in a simplified controlled setting using synthetic data, before we incorporate field data gathered at a seismic exploration site in an area containing several roads, wind turbines, oil pump jacks and railway traffic. Across diverse scenarios, the model demonstrates proficiency in learning the transfer function among various seismic station configurations. Particularly, it achieves high accuracy in predicting a majority of seismic wave phases across different datasets. Diverging significantly from encoder-decoder networks that estimate time series forecasts by analysing historical trends, our approach places greater emphasis on the wave propagation between nearby locations. Thereby, the analysis incorporates both phase and amplitude information and provides a new approach to approximate the transfer function relying on Machine Learning techniques. The gained knowledge enables to reconstruct data from missing, offline, or defunct stations in the context of temporary seismic arrays or exclude non-relevant data for denoising.

1. INTRODUCTION

Signal recording and processing hold significant importance across a range of scientific disciplines, including the field of geophysics. Capturing and analyzing various types of signals, such as seismic waves, electromagnetic waves, and gravity anomalies, enables the understanding of the Earth's subsurface and its geological characteristics. As waves propagate through the Earth, their interaction with geological structures, such as sediment layers or fault lines, affects the recorded signals and leads to changes in the wave's propagation characteristics. Deploying seismic stations enables the measurement of signals and the derivation of insights regarding the subsurface characteristics and nature of the area.

In seismic analysis, understanding these measurements involves the identification of different wave types, along with analyzing frequency spectra, amplitude variations, phase shifts, and other wave properties (**M. Bath, 1973**; **Rost and Thomas, 2002**; **Barnes, 2007**). While many of these signal components deliver valuable information and are essential for seismic investigations, there are also parts known as seismic noise that introduce more complexity to the data interpretation process. Natural sources such as wind or ocean waves, atmospheric disturbances, or geological activities, as well as artificial sources including human activities and industrial operations, emit noise signals in various frequency bands and contribute to seismic measurements. In order to interpret measurements and mitigate the influence of undesired signals on the results, understanding the relationship between input and output within a given physical system is essential (**Walden and White, 1998**; **Kawakami and Oyunchimeg, 2003**). The transfer function, denoting this relationship, holds significance across multiple disciplines, including the field of seismology. For instance, the relation between the ground motion and the recorded seismogram is named instrument response (**Havskov and Alguacil, 2016**; **Lindsey et al., 2020**), while the relationship between ground motions at different points is called Greens function (**Snieder, 2004**; **Sabra et al., 2005**; **Sergeant et al., 2020**). However, estimating the transfer function in seismology can be complex due to the interaction of varying subsurface structures, variability in seismic wave propagation, noise and instrumentation limitations leading to complex coupled systems of differential equations.

Machine Learning has emerged as a widespread methodology in geophysical data analysis, providing an advanced alternative to conventional seismic analysis methods for uncovering relationships within seismic data. Multiple fields including seismic exploration (**Helmy et al., 2010**; **Li et al., 2019**; **Tariq et al., 2021**) and seismology (**Li et al., 2018**; **Xie et al., 2020**; **Mousavi and Beroza, 2023**) employ Machine Learning methods to characterize seismic data and detect and classify relevant characteristics and patterns within the data. One fundamental architecture in the subfield of Deep Learning (**LeCun et al., 2015**) are encoder-decoder networks, which provide the opportunity to learn and extract dependencies between data across input and output domains. In seismic and seismological applications, encoder-decoder networks play a crucial role for tasks like denoising (**M. Saad and Chen, 2020**; **Knispel et al., 2022**; **Yin et al., 2022**) or interpretation (**Wu et al., 2019**; **Zhang et al., 2021**).

In this paper, we introduce an adaptation of encoder-decoder networks to learn the relationship between seismic wave fields recorded at two different locations. By using one dimensional time series from a fixed seismic station as input and the measurements from a nearby seismic station as target, we aim for the network to learn the alterations that the signal undergoes between the two stations. Through this approach, we want to demonstrate that a modification of the encoder-decoder architecture is capable of learning data characteristics that closely resemble the principle of the transfer function within the setup of two seismic stations. While the foundation of the concept originates from the established practice of detecting and learning patterns and structures of and within time series data (**Malhotra et al., 2016**; **Badrinarayanan et al., 2017**; **Du et al., 2020**; **Beveren et al., 2023**), our approach focuses more on the parts that influence the propagation of waves between nearby locations. Thereby, the analysis incorporates both phase and amplitude information and provides a new approach to approximate the transfer function using Machine Learning techniques. By considering phase information, our approach distinguishes from Wiener prediction filters.

We will guide through this study by introducing the encoder-decoder network setup and the most important metrics for this specific use case (Section 2) first. Following this, Section 3 outlines the characteristics of the measurement region and provides an overview of the selected seismic stations and data. Section 4 will involve evaluating the findings across different scenarios and datasets before discussing (Section 5) and drawing conclusions on the potentials and limitations of the presented method (Section 6).

2. NEURAL NETWORK SETUP

The methodology employed in this study follows the overall aim of testing the feasibility of a network that is able to learn the transfer properties between two seismic stations. We make use of an encoder-decoder architecture in a supervised fashion and train it by using input data from a fixed reference station A and target data from a second station B (Figure 1, top). The form of the network traces the traditional U-Net shape (**Ronneberger et al., 2015**; **Zhu and Beroza, 2019**; **Zhong et al., 2022**; **Li et al., 2022**) while an equal amount of convolutional and deconvolutional blocks defines its structure. Each block consists of a convolutional layer, a batch normalization layer and an activation layer. Furthermore, we use a dropout layer after each block to prevent overfitting by randomly setting a fraction of input units to zero during training. To make sure that every input connects to every output, we extend the architecture by a dense layer in the latent space bottleneck. To enable the direct transfer of information from the encoder to the decoder, we introduce skip connections between the respective convolutional and deconvolutional blocks. The depth of the network is five, while we use hyperbolic tangens as final activation layer in each of the individual use cases introduced in Section 3. As an outcome of the learning process from the input to the target data, the network delivers a prediction that ideally resembles the shape of the target data. Figure 1 illustrates the schematic network architecture subdivided into the use of input and target data, the encoder part, the latent space, and the decoder part.

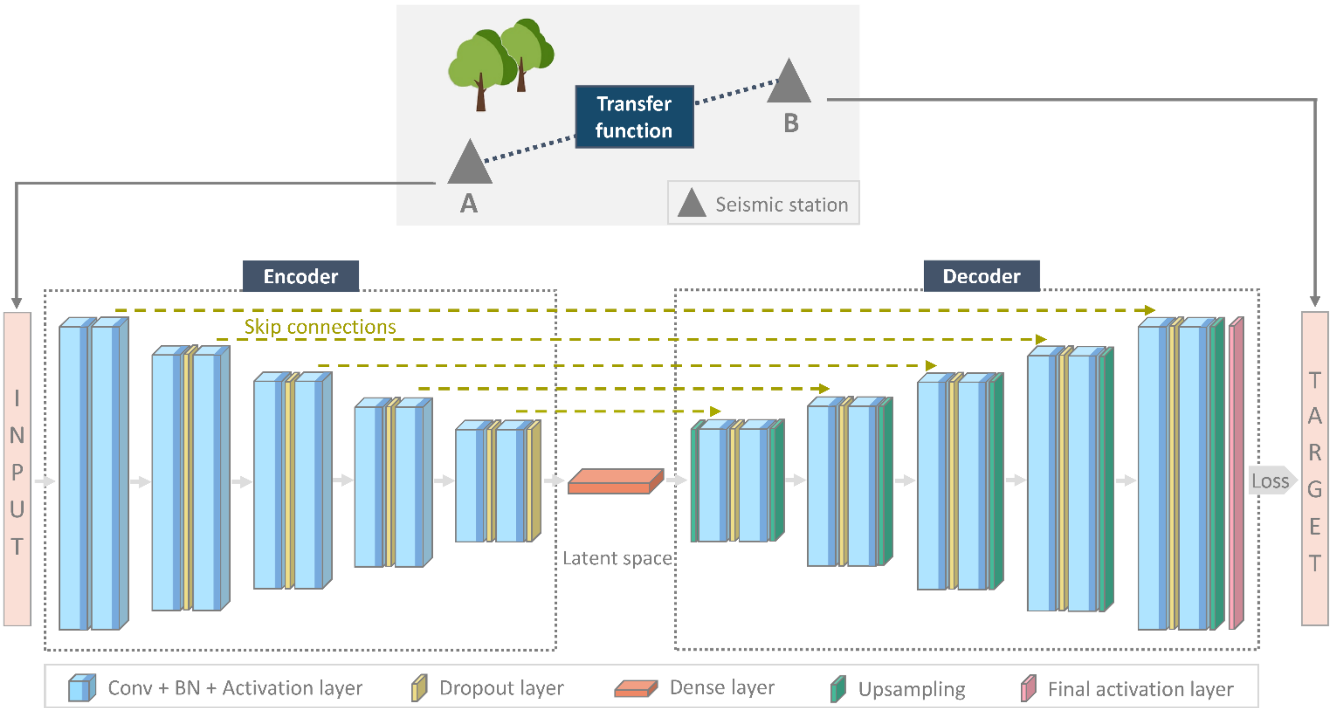

Figure 1. Simplified visualization of the network architecture consisting of an encoder and decoder part. Data from seismic station A serve as input, while data from another seismic station B provide the target data. Skip connections (olive dashed lines) link corresponding convolutional and deconvolutional blocks. Within the encoder, each block consists of a Convolutional layer (Conv), Batch Normalization (BN) and an Activation layer. A dropout layer follows almost every block. Within the decoder, each block with dropout layer complements by an Upsampling layer.

To assess the model performance, we select different metrics to evaluate the similarity between the predicted ($\hat{y}$) and the observed value (y). In order to optimize the model during the training process of the algorithm, the error between the model prediction and the actual target data is estimated using the Huber loss function implemented by Keras (**Chollet and others, 2015**). The Huber loss l (Eq. (1)) combines the mean squared error (MSE) and the mean absolute error (MAE) with ∂ defining the threshold for the transition from quadratic to linear components of the loss. This helps the Huber loss function to be robust to outliers in the data.

$$l(y,\hat{y}) = \begin{cases} \frac{1}{2}(y-\hat{y})^2 & \text{for } |y-\hat{y}| \leq \partial \\ \partial\left(|y-\hat{y}| - \frac{1}{2}\partial\right) & \text{for } |y-\hat{y}| > \partial \end{cases} \tag{1}$$

To evaluate the performance of the model and the goodness of its prediction after training is finished, we select two metrics to independently assess both amplitude and phase fit, and subsequently consider them in equal measure for an overall indication of the model quality.

In order to assess the degree of similarity between the target and prediction time series, one evaluation metric of choice is the normalized cross-correlation function. This function measures the similarity between the two time series based on the displacement of one relative to the other and normalizes by the overall standard deviation. While phase shift in seismology denotes the time displacement of a waveform, we employ this metric to emphasize the temporal alignment between the two signals. Assuming a good model and thus an accurate prediction, we expect both signals to be identical and align well without any offset. Under this assumption, we compute the cross-correlation without shifting samples and determine the cross-correlation coefficient at time zero. By doing so, a value of 1 indicates a strong positive similarity, -1 indicates an anti-correlation, and 0 reflects no relationship between the two time series. Assessing the cross-correlation on the entire time series as well as in smaller segments of about 10.24s helps in determining the quality of the results in detail.

Classifying the amplitude differences between the predicted and the actual target values, the Root Mean Squared Error (RMSE) quantifies the accuracy of a model while being sensitive to the magnitude of errors. Thereby, the RMSE indicates how far the predicted value deviates from the target value. Employing RMSE as the second evaluation metric aids in comparing the amplitudes of the actual target data with those predicted by the model. It defines as shown in Eq. 2, where n represents the total number of data points and i refers to the i^{th} observation. With increasing errors, the RMSE score tends to rise linearly, indicating that a smaller value corresponds to a closer alignment between the model's predictions and the actual data. Thereby, RMSE shares units with the actual target values.

$$RMSE = \sqrt{\frac{1}{n} \sum_{i=1}^{n} (\hat{y}_i - y_i)^2} \tag{2}$$

While the Huber loss is estimated as part of the model training process to enhance the models understanding of the data iteratively, cross-correlation coefficients and RMSEs are calculated post-training. Estimating both provides a comprehensive approach to quantify the model's predictive capability of how well it captures the phases and amplitudes of the target data. Thereby, we do not combine the metrics numerically, but rather use them to comprehend the quality of the results.

3. DATA AND PROCESSING

In order to demonstrate the viability of the proposed method in capturing the relationship between two seismic stations, we will employ one-dimensional time series measurements, starting with the exploration of synthetic data. With this, we aim to validate the viability of the general approach in a controlled setting, before we proceed to analyze field data gathered during a seismic exploration campaign.

Synthetic data

To generate synthetic data, we simulate two seismic stations with a constant interstation distance of 200m located on top of a homogeneous, acoustic half-space. Initially, we create an ideal scenario with a single source, always coming from the same direction, located near the stations but changing its location for each example (Figure 2(c), S1). The Green's function is a time series with a value of one at the given travel time, zero elsewhere, and a time offset due to the interstation distance. By generating morlet wavelets and convolving them with the previously described time series, we are able to generate surface waves that are not undergoing any reflections, refractions, or conversions. As a result of activating the source only once, we receive a simplified time series that contains a single wavelet at a specific travel time. In order to resemble real-world setups with multiple ambient noise sources more accurately, we increase the complexity of the setting by incorporating 20 randomly distributed sources into the scenario and dispersing them with varying spacing around the station pair (Figure 2(c), S2). While keeping the position of the sources stationary, we introduce some sources activating multiple times with varying offsets for each of the active sources. This results in a time series of overlapping signals from various distances and directions. To stabilize the procedure, we further add random noise to the data of both scenarios. Furthermore, we establish identical initial conditions for the model training through the generation of an equivalent amount of synthetic data compared to that present in the field data measurements.

Field data

To evaluate the applicability of the proposed method across various data scenarios, we employ not only synthetic data but also incorporate field data gathered at a seismic exploration campaign conducted by the OMV E&P GmbH in the Vienna basin, Austria. The array setup consisted of in total 4907 seismic stations, each tooled with either 12 or 24 geophones (vertical components), and spaced with an interstation distance of approximately 200m (Figure 2(a)). The measurement period comprises a total duration of about four weeks during March and April 2019 using a sampling rate of 100 Hz. Major and minor roads surround and intersect the region, and a railway line runs along its southern boundary. In addition to these sources of seismic signals, wind turbines and oil pump jacks appear throughout the region (Figure 2(a)). The wind parks Prottes-Ollersdorf and Grossengersdorf are situated northeast and southwest within the array, while the wind park Deutsch-Wagram is located on its southwestern boundary. Oil pump jacks position in various setups, ranging from individual placements to small clusters and larger groupings within the array. Ocean noise reaches the stations predominantly from the northwest direction. **Schippkus et al., 2022** provide another detailed description of the array used in this study. The authors explore the impact of an isolated noise source within the framework of seismic interferometry using the same dataset. Furthermore, a detailed description of the study area offering background information on the present industry and additional potential sources of noise is given by **Schippkus et al., 2020**. While using a different array than the one in this study, the authors provide detailed insights into the source characteristics of the region by examining spectrograms and power spectral densities.

For the model training, we select three station pairs within the southwestern quarter of the array. The choice of station pairs thereby depends on the respective area conditions in terms of wind turbine and oil pump jack distribution and the distances of these sources to the stations. We successively enhance complexity between the scenarios by increasing the number of surrounding noise sources and consider their spatial proximity to the stations. We evaluate the close vicinity of a wind park in absence of other sources, as well as configurations with and without a wind turbine positioned directly between the stations. Figure 2(b) shows the three scenarios and their surrounding noise sources. The first station pair F1 situates at the western edge of the array in an area surrounded by fields. The wind park Grossengersdorf is located in the southwestern vicinity of the stations, having its closest wind turbine east of the stations in about ~110m to the target station and ~250m to the reference station. Situated more towards the center of the array, the second station pair F2 encircles by wind turbines and oil pump jacks, appearing either individually or in smaller groups. With a distance of ~55m to the reference station and about ~125 m to the target station, a single wind turbine locates between the stations. For the third station pair F3, the number of surrounding sources further increases, particularly witnessing a greater number of oil pump jacks in close proximity to the stations. In contrast to the other station combinations, there is no wind turbine directly next to the stations in this case. The closest wind turbine is located at a distance of about ~440m, while the nearest oil pump jack is ~950m away. To ensure an appropriate and consistent amount of training and testing data, we limit the measurement of each station to a period of two days.

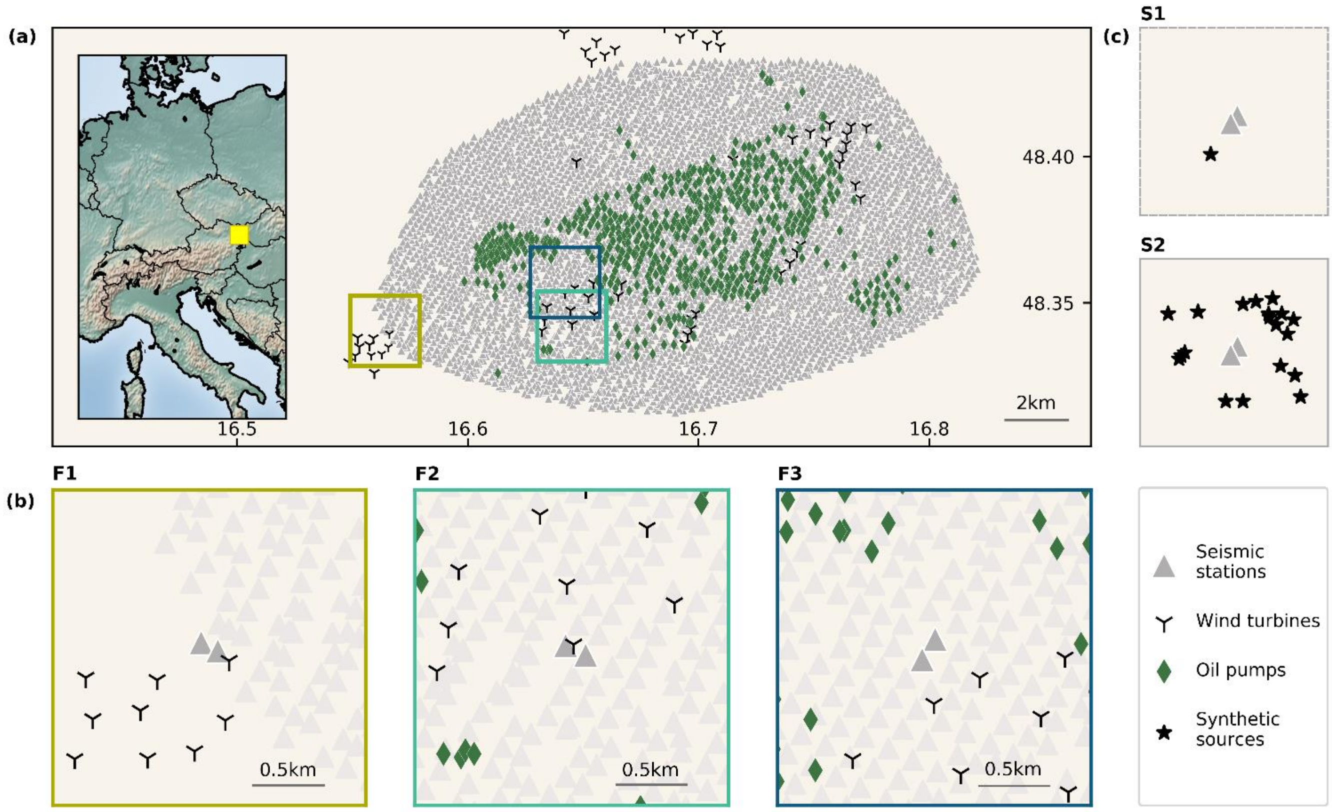

Figure 2. Geometry of the experiment and synthetic setups. (a) Map of the study area northeast of Vienna, where seismic stations are positioned with an interstation distance of approximately 200 m. The chosen pairs of analysed stations are indicated by colored boxes (olive, cyan, dark blue). (b) Detailed view of the three chosen station pairs F1, F2, and F3 from the array deployment. The plot's border color corresponds to its location on the map. (c) Configuration of synthetically generated station pairs S1 and S2 with surrounding sources.

3.1 Data processing and model training

Prior to starting the training of models for each of the datasets, it is essential to perform pre-processing on the data, as it directly impacts the network's ability to learn accurately. In addition to filtering the data below 10Hz using a Butterworth low-pass filter, data preparation for both synthetic and field data includes the alignment of all amplitudes to the same range through data scaling. For the synthetic data, we implement normalization to consistently scale the data within the range of [-1, 1]. Given the data generation process, we expect only minimal variations within the data, thus eliminating the need for independent centering and scaling using standard scaling methods. With regard to the variety of sources influencing the characteristics of the field data, we anticipate greater variations in range and distribution within this dataset. Therefore, we combine both standard scaling and normalization to account for these variations. Initially, standard scaling is applied to center the data around zero and standardize its deviation to one, followed by normalization to adjust the data to fit within the range of [-1, 1]. Before scaling, we allocate 80% of the data to the training set and 20% to the testing set. Additionally, 20% of the training data is automatically determined as the validation set during model training. To ensure successful model training, it is important to provide a sufficient amount of training and testing examples. To do so, we divide the overall time series of two days into chunks of 10.24 seconds each, while each chunk corresponds to 1024 samples based on a sampling rate of 100 Hz. Like this, we receive 13.500 chunks for training and 3.375 chunks for testing. In the following, we will refer to these chunks as traces.

We train our encoder-decoder model using pre-processed input traces from reference station A and provide the traces from station B as the target we aim to predict. This way, we obtain a unique model for each station pair that outputs predictions based on the individual dataset provided. Subsequently, we compute relevant metrics between the target and prediction to assess the model performance. Following architectural investigations, we empirically determine the optimal network depth by analyzing accuracy, convergence and model performance on a sample of the data before starting model trainings. In order to capture the complexity of the data and avoid overfitting, we use a network depth of five layers. Figure 1 shows the schematic layout of the network having five convolutional and deconvolutional blocks. We train our models with a learning rate of 10^{-4} for 1500 epochs each, as further training beyond this point does not significantly improve performance.

4. RESULTS

Following the training phase, we evaluate the models by calculating the Root Mean Square Error (RMSE) and cross-correlation coefficient (CC) between the target data and the corresponding model prediction. We assess both metrics on the overall target time series of two days, and on smaller segments of it. To facilitate the analysis of results and improve the visual representation, we analyze our results within output segments that are half the size (512 samples) of the training and testing traces. When the model captures all relevant transfer features from the data, its predictions will accurately correspond with the unseen target data. To scrutinize the results in terms of positive and negative amplitude deviations, we visualize each sample of the entire target time series against the model prediction by density plots (Figure 3(d)). In order to comprehend the correlation dynamics across the whole dataset, we further estimate correlation coefficients for each window of 512 samples without any shift and visualize their distribution through a histogram (Figure 3(e)). Going into further detail, we will analyze a representative example trace (Figure 3(b)) for each scenario along with its corresponding prediction, correlation coefficient and input data (Figure 3(a)) from the model training. To understand how the cross-correlation coefficient evolves throughout the data, we link each section of the trace to its corresponding correlation coefficient, as shown in Figure 3(c). For this, we compute these correlation coefficients using moving intervals of 20-sample windows with a 10-sample offset and visualize the results.

4.1 Synthetic data

Figure 3 illustrates the results for the two scenarios of synthetic data. For the single source case S1 (Figure 3(a)-(e)), the model prediction closely aligns with the actual target data (Figure 3(b)), showing the algorithm's general capability to predict the transfer properties in a very simplified setup. Metrics support this observation, validating the accuracy of predictions and the presence of minimal errors by a small RMSE value of 0.04. While the majority of value pairs cluster around the ideal case of correct amplitude predictions as indicated by the dotted purple line in Figure 3(d), some segments show significant deviations, highlighting instances where the prediction does not align with the target values. The overall cross-correlation coefficient of 0.90, as shown in Figure 3(e), reflects the predominance of good fits, though it moderates by the occurrence of some less accurate predictions. The histogram shows, that a majority of traces display a correlation coefficient close to one, while another distinct cluster is observed around zero. We attribute the latter cluster, observed around zero, to the random noise introduced in the data, which adds variability but does not necessarily indicate a systematic relationship. Consequently, the predictions do not align with the target, leading to CCs near zero. This observation is confirmed by the analysis of CCs in smaller windows (Figure 3(c)), which indicate strong correlations when predicting the wavelet at given travel time, whereas the correlations of random noise components are significantly lower.

The presence of 19 sources surrounding the stations (S2, Figure 3(f)-(j)) introduces increased variability to the data, evident in the time series as overlapping signals with varying amplitudes (Figure 3(g)). While certain segments of the target trace align with the model predictions (Figure 3(g)), other parts reveal disparities in either amplitude or the general shape of the wavelet. The overall correlation coefficient of 0.34 (Figure 3(j)), along with the RMSE of 0.13 (Figure 3(i)) highlights larger differences in the similarity of the time series compared to the single source case S1. However, the given overall correlation coefficient of 0.34 indicates a predominantly positive correlation, implying that the model is able to approach a modest similarity between its predictions and the target data. The analysis of the correlation coefficients for individual traces (Figure 3(j)) reveals characteristics of Gaussian-like distribution, with the majority of values concentrated between 0.1 and 0.4, and some traces reaching an upper limit near 0.8 and a lower limit around -0.4. Analysing the kind of differences between the target and predictions (Figure 3(i)) demonstrates a slightly tilted elliptical shape of amplitude mismatch around the center indicating that amplitudes are more commonly underestimated than overestimated.

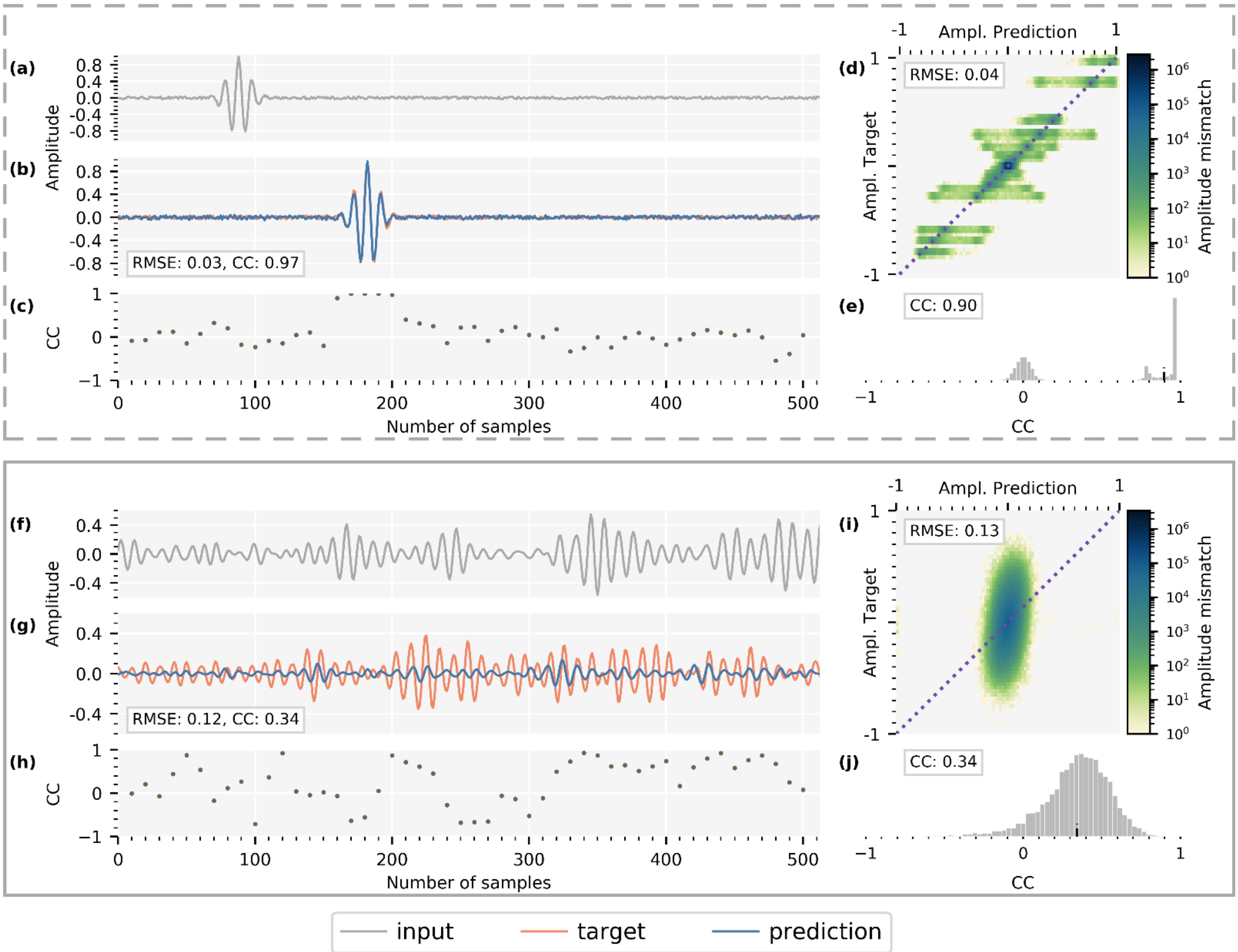

Figure 3. Results of the model analysis for two synthetic data scenarios (S1, top - dashed grey box; S2, bottom - solid grey box) using Root Mean Square Error (RMSE) and cross-correlation coefficient (CC) across the entire target time series and within traces. The light grey line represents the input data ((a), (f)), orange and blue lines denote the target and network prediction respectively ((b), (g)). The density plots ((d), (i)) show the network prediction of the target against the actual target data, while the dotted purple line visualizes the ideal best-fit line for the regression. Single grey points ((c), (h)) depict cross-correlation coefficients for 20-sample sections beneath the corresponding example trace. Histograms ((e), (j)) show correlation coefficients for windows of 512 samples each. The black marker highlights the overall correlation coefficient of the entire time series given in the text box.

The outcomes from both scenarios reveal promising indications of the feasibility of this model architecture. While they exhibit significant differences in performance, both models generate predictions that indicate patterns, for example, predicting phases accurately rather than appearing random. Especially scenario S1 thereby demonstrates the potential of the overall algorithm to learn the transfer between two nearby stations, despite not accurately representing real-world conditions. Even in the second scenario, the prediction maintains a reasonable level of accuracy. This establishes a solid foundation for the transition to field data, mirroring a comparable scenario where two seismic stations are encircled by seismic sources.

4.2 Field data

Figure 4 depicts the outcomes for the three field data scenarios. Beginning with the first station pair located at the array's edge near a wind park (F1, Figure 4(a)-(e)), the model prediction closely aligns with the actual target data in various segments (Figure 4(b)). While we observe positive and negative deviations in amplitudes between target and prediction in several parts of the trace, the prediction of phases exhibits accurate matches with the target time series. Figure 4(c) confirms this observation, as the correlation coefficients for the majority of trace subparts cluster near one, highlighting the model's accuracy in predicting phase information. With an overall correlation coefficient of 0.75, the concentration of individual correlation coefficients (Figure 4(e)) is mostly within the positive range of 0 to 1, having its peak strength at a high correlation value of around 0.8. A cluster of values around 0.75 characterizes the central tendency of the dataset and emphasizes further the models ability to make predictions of similarity to the target data. Besides, there is another notable peak around -0.58 and -0.78, likely attributable to data gaps present in this dataset leading to inaccurate predictions in the negative range. Evident from the elliptical shape, the density plot (Figure 4(d)) reveals positive and negative mismatches of amplitudes along the dotted purple best-fit line. Thus, both positive and negative amplitude predictions display tendencies of overfitting and underfitting, reflecting some variability in the model's capacity to accurately estimate amplitude values. The RMSE reflects this with an average deviation of around 0.13 units of amplitude between predicted and actual values. In comparison to previous examples, this scenario indicates a relatively broader distribution of amplitude values stretching to the lower and upper limits of the data range.

While wind turbines are already in close proximity to the stations in the first case F1, the distance further halves for the second scenario F2 ((Figure 4(f)-(j)), where a wind turbine is located directly between both stations. Although the overall correlation coefficient of 0.77 (Figure 4(j)) is nearly identical to the one of the previous example, there are visual differences regarding the data itself and the model outcomes leading to variations in the results. Examining the example trace (Figure 4(g)), the predicted phases largely correspond with those of the target data again. The predominance of correlation coefficients close to one supports this observation (Figure 4(h)), although minor or negative coefficients occur occasionally. However, the amplitude predictions again exhibit greater variances compared to the targets. While the RMSE for the selected trace is 0.06, the global RMSE measures at 0.08 (Figure 4(i)), indicating more accurate amplitude predictions for this station pair compared to case F1. This is also evident when looking at the distribution of values around the purple dotted best-fit line of the plot. Similar to the initial example, the analysis reveals a tendency to both over fit and under fit, affecting the accuracy of predictions for both positive and negative amplitude values. However, the dataset predominantly consists of smaller values, leading to reduced variability and a narrower range of data dispersion. Following this, the individual correlation coefficients of traces (Figure 4(j)) not only approximate a nearly Gaussian distribution again but also display increased steepness, indicating a tighter clustering of values around the mean.

The third station pair, F3, unique among the combinations as it lacks a wind turbine in direct proximity to the stations, leads to an overall correlation coefficient of 0.58, as shown in Figure 4(o). Although the overall correlation coefficient represents a decrease relative to those found in earlier field data examples, the amplitude deviations, characterized by an RMSE of 0.10, lie within an intermediate range compared to the observations from the prior two cases. In this instance, as shown in Figure 4(n), the comparison of target and predicted amplitudes reveals an elliptical shape again. However, the ellipse appears more circular in comparison to previous cases, suggesting that it represents an intermediate scenario in terms of the spread and steepness. Additionally, there is the same tendency of over- and underestimation as in previous scenarios. The analysis of the model’s performance on the example trace (Figure 4(l)) shows disparities between the target and predicted values in certain intervals, whereas other sections align well. Correlation coefficients, derived from 20-sample segments of the example trace (Figure 4(m)), confirm this impression: values near one mirror precise phase predictions or moderate amplitude fits, while values at or below zero point to negative predictions. The analysis of correlation coefficients for trace windows (Figure 4(o)) reveals that most bins lie within the positive range of 0.2 to 0.8, while we identify one large peak above 0.9. This indicates the presence of a generally positive linear relationship between input features and the models output predictions, affirming the model's effectiveness in detecting data patterns to a certain degree.

All three field data examples exhibit moderate to strong linear correlation, providing predictions that resemble the actual target to a high degree. In this regard, both the visual assessment and the evaluation metrics surpass the performance of the second synthetic example S2, which mirrors comparable environmental conditions of having sources distributed around the stations. However, the field data examples do not achieve the level of accuracy seen in the perfect synthetic case S1, suggesting that the performance of field data models ranges somewhere between these two extremes. Physically, we also expect the source regime to be a hybrid between single source and evenly distributed sources, with a tendency towards a few significant sources.

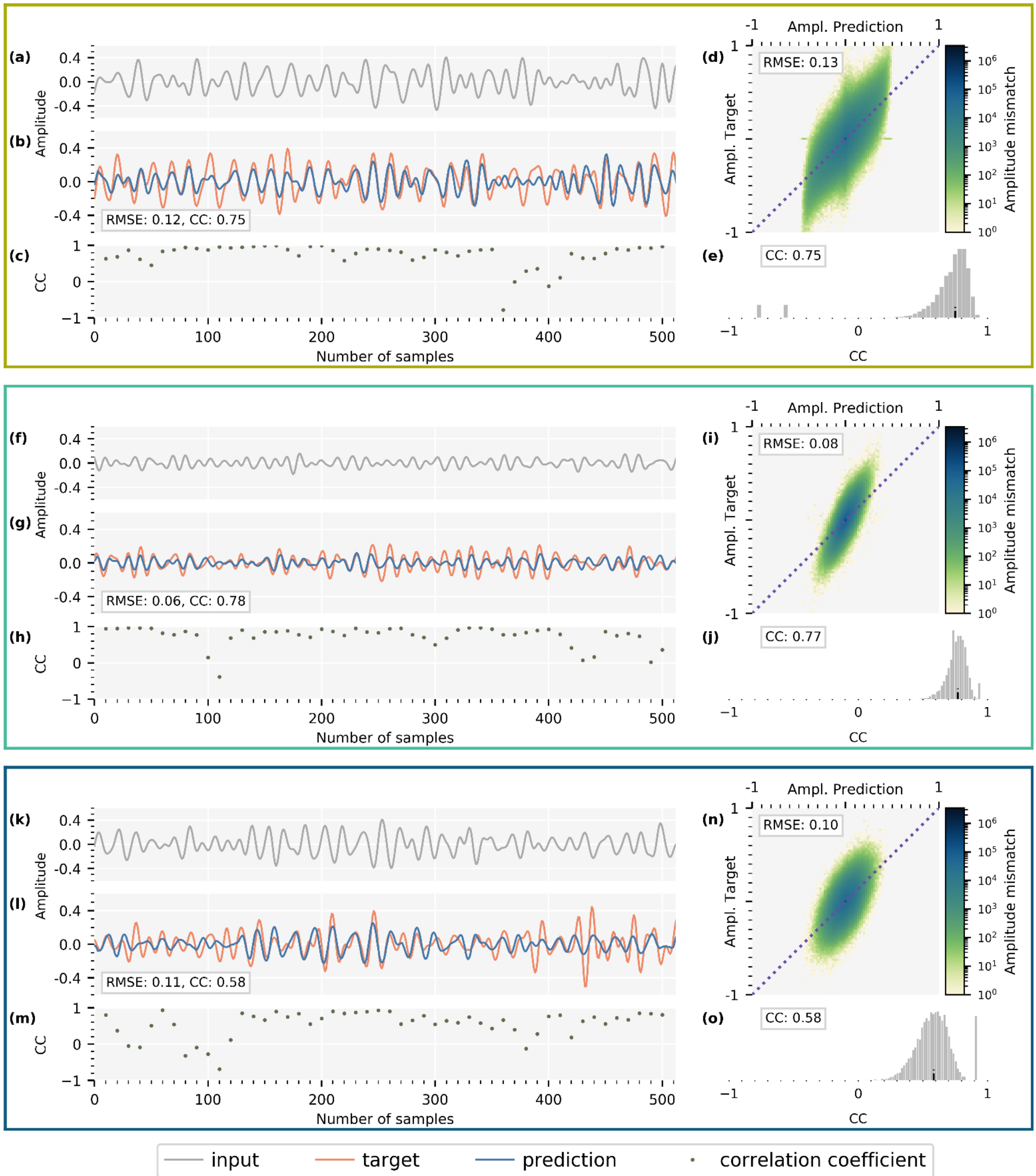

335

Figure 4 Results on the comparative analysis (cf. Figure 3) for three field data scenarios (F1 top, F2 middle, F3 bottom). 336
Plots provide insights into the examination of correlation dynamics, magnitude deviations, and distribution patterns 337
using Root Mean Square Error (RMSE) and cross-correlation coefficient (CC) for evaluation. The results for this dataset 338

follow the same evaluation criteria and presentation as in Figure 3. The frame color of the box indicates the corresponding scenario.

5. DISCUSSION

The model architecture described in this study shows the capability to predict the transfer properties, in our case the 1D time series, between two seismic stations in different source-station-setups. Employing diverse scenarios of both synthetic data (Figure 3) as a controlled environment, and field data (Figure 4), representing real-world conditions, delivers a comprehensive proof of concept across different datasets. Overall, the models demonstrate strong predictive performance, particularly in predicting the phase of the wave field more reliably than its amplitude, as demonstrated by both synthetic (Figure 3) and field data examples (Figure 4). While the models manage the novel scenario of differing input and target data effectively, further optimization by fine-tuning various factors, such as hyperparameters, could affect the algorithms performance even further (**Weerts et al., 2020**; **Yang and Shami, 2020**; **Bakhashwain and Sagheer, 2021**).

Particularly evident in the scenario S1 (Figure 3(a)-(e)), the model training benefits significantly by considering only a single source from one direction and random noise, representing an idealized scenario. This simplification yields favourable results, underscoring the network's general ability to learn a given relationship in a controlled setting. Moving to scenario S2, the approach handles a higher level of complexity introduced by simultaneous inputs from multiple directions. Despite these challenges, the algorithm maintains a decent level of performance, as evident by the mean correlation coefficient (CC) of 0.34. When comparing the performance of this second synthetic example S2 (Figure 3(f)-(j)) with that of the field data models, all results from the field data exceed the performance observed in S2 with CCs of 0.58, 0.75 and 0.77. Although scenario S2 may seem initially favourable due to the uniform energy propagation from the synthetic sources, the observed performance improvement in the field data is likely driven by the unique characteristics of different sources around the array, such as wind turbines, oil pumps or roads. Despite similarities in source distributions between the two setups, our field data do not exhibit the extreme conditions of S2, demonstrating the robustness and practical applicability of our approach in more natural and realistic scenarios.

While the CC threshold values we obtain might be considered relatively low or almost comparable in the context of some ML studies (**Wu et al., 2021**; **Verma et al., 2024**), in seismology, **Schaff et al., 2002** used a normalized CC of 0.7 as a criterion for reliable relative arrival time measurements. **Wegler and Sens-Schönfelder, 2007** considered only cross-correlation coefficients above 0.5 for their dv/v analysis, and **Castellanos et al., 2020** only use travel time measurements with CCs larger than 0.5 as reliable. Although the research settings of their studies differ from ours, the range of values of CC thresholds in “real data” studies underscores its broad applicability as a measure of data reliability. This alignment emphasizes that our use of noise field data is yielding results that are comparably robust and reliable.

In addition to the equal distribution of energy for each source in the synthetic data scenarios, the inconsistent and repeated activation of these sources may fail to generate learnable characteristics in the dataset. The absence of pattern-like attributes introduces challenges for the algorithms learning process, as they represent essential relationships within the data that models are trained to learn and utilize. While this could potentially create challenges with our synthetic data, the situation shifts with the nature of sources present in the field data, which exhibit consistent and repetitive signals. Given the distribution of surrounding sources in the field data examples (Figure 2 (b)), we account for the presence of wind turbines at various distances in each scenario. **Neuffer et al., 2019** demonstrate that wind turbines show directional characteristics with wind-dependent specific patterns. Anticipating these sources to introduce distinct patterns by the propagation of similar signals, we expect them to provide valuable input to the model training and enhance its predictive accuracy. Given that our results improve when wind turbines are in close proximity to the stations, the presence of such noise sources appears to resemble the characteristics of a single source and thus positively influences the model’s performance.

While it is evident that consistently emitting sources such as wind turbines positively impact our results, it is not immediately clear why we observe stronger accuracy across various datasets in the prediction of phases, while our models preferentially underestimate amplitudes (Figure 3, Figure 4). Given that neither the area of investigation nor the characteristics of the sources and stations indicate any physical phenomena that could account for these deviations, it appears that there are no evident physical processes to explain this behaviour. Consequently, we will focus our investigation on the data as well as the architecture and parameters of the models as potential cause. The fundamental nature of encoder-decoder networks, particularly autoencoders and the ones used for sequence-to-sequence learning, aims to capture and reconstruct patterns in the data. However, these networks learn to prioritize certain characteristics of the data based on their architecture, parameters and data attributes. Upon visually inspecting our data, it becomes apparent that the spacing between phases of our time series appears to be relatively consistent. This can be attributed to two key factors: the application of filtering and the dominance of a relatively narrow frequency band in the remaining frequencies. While this is true for the phases, amplitudes vary between high and low values and span from positive to negative, which poses a greater challenge for the model to learn the data properties. Besides the architecture of encoder-decoder networks and the quality of training data, the choice of parameters like learning rate, batch size and loss function can affect the model performance, yet demands additional research for a comprehensive understanding.

Although it is not obvious to us why amplitudes are preferentially underestimated, many seismological applications rely entirely on the phases of seismograms. Our models reliably predict the phase of seismic noise. For instance, phases from seismic waves are essential for determining arrival times of different waves, which help to locate earthquake epicentres and understand Earth's internal properties. In addition, phase-based investigations, such as ambient noise tomography and seismic interferometry, predominantly rely on phase information to extract subsurface details. As highlighted by **Bensen et al., 2007**, ambient noise data processing involves steps like cross-correlation and temporal stacking, which are inherently phase-dependent, and the accurate measurement of dispersion curves, which utilize phase and group speeds. Seismic interferometry, for example, involves the cross-correlation of seismic recordings at different stations, allowing researchers to reconstruct the Green's function between two points using phase information. This highlights that while our amplitude predictions may be less precise, the critical phase information remains robust and useful for various seismological analyses.

In general, choosing an encoder-decoder architecture suits the requirements of the given problem, as it is able to capture complex relationships and generalizes well to unseen data. Traditionally, this approach is used to predict future values of time series based on historical trends, using past data as input to forecast subsequent values within the same series. Using it with input data from one seismic station and target data from another seismic station thereby diverges from this conventional application as well as from classical autoencoders. While autoencoders aim to learn a compressed representation of the input data, the proposed architecture extends this approach to learn and predict the relationship between data from distinct stations. In other words, our model learns the propagation of complex wave fields between the stations. This allows to model spatial and temporal dependencies between seismic data relying on the phase and amplitude information of the signals. One might draw parallels between this approach and Wiener prediction filters (**Chen et al., 2006**; **Chandra et al., 2014**), which also aim to capture dependencies within signal data. However, it is important to note that Wiener prediction filters primarily deal with the auto-correlation of signals, focusing on their power spectrum without considering phase information. Wiener filtering assumes non-deterministic signals, which contradicts seismic signals known for their deterministic nature, such as reflections from layered structures. In contrast, our method comprehensively accounts for the dynamic, non-linear interactions and phase information essential for accurately modeling wave propagation in seismology.

To advance our approach from the proof-of-concept stage described herein to concrete applications, several aspects will likely need to be addressed. These could encompass technical and structural enhancements that include the improvement of data quality, fine-tuning of hyperparameters or the accuracy of amplitude predictions. Additionally, we might consider adjustments to the synthetic data generation process to better resemble conditions encountered in field environments with multiple ambient noise sources. Future studies might also delve into how the geographical and spatial configuration of sources and receivers impacts the results. Given the differences in model performance in predicting phases and amplitudes, experimenting with different model architectures and parameters could further be advantageous. By implementing these modifications to the model setup and understanding influences on the results in detail, we can further refine the overall performance and robustness of our approach.

6. CONCLUSION

In this study, we have successfully presented and tested an adaption of encoder-decoder networks to predict the transfer function of seismic wave fields, between two seismic stations. By introducing one-dimensional time series data from a fixed seismic station as the input to the network and data from a nearby station as the target, our approach effectively learns the transfer function between the locations. Initially tested with synthetic data, the approach was validated further with field data from a seismic exploration campaign. Employing a range of scenarios with varying surrounding conditions – from a controlled environment with synthetic data to field data including several sources of ambient noise - we demonstrate a broad proof of concept.

Our findings confirm that our approach effectively predicts the wave field recorded as time series at a seismic station using input from a neighbouring seismic station, resulting in machine learning models with varying degrees of accuracy. Notably, our models not only achieve high precision in predicting the phases of seismic waves but also perform adequately in estimating amplitudes, demonstrating significant potential for the field of geophysical research. This makes our approach particularly valuable for applications requiring precise seismic isolation or compensation, such as active vibration isolation in photolithography, semiconductor manufacturing, and 3D-microfabrication (**Kerber et al., 2007**; **Kim et al., 2009**). It is also highly relevant for projects like the Einstein Telescope (**Punturo et al., 2010**; **Harms et al., 2022**), where extremely sensitive gravitational wave detections need to be free from seismic disturbances. Additionally, our approach also opens up the potential for the novel concept of virtual seismic arrays.

Author Contributions

Jana Klinge: Conceptualization, Data curation, Formal analysis, Investigation, Methodology, Software, Validation, Visualization, Writing – original draft, Writing review & editing

Sven Schippkus: Conceptualization, Data curation, Supervision

Jan Walda: Conceptualization, Software

Celine Hadziioannou: Conceptualization, Funding acquisition, Supervision

Dirk Gajewski: Conceptualization, Funding acquisition, Supervision

All authors have read and agreed to the published version of the manuscript.

Data Availability Statement: The data underlying the findings of this study were provided by OMV Exploration and Production GmbH. Restrictions apply to the availability of these data, which were used under license for this study. The color scheme utilized for the scatterplots in this study was sourced from **Crameri, 2023**. The color scheme for the frames used to emphasize the selected station pairs was taken from **Tol, Paul, 2021**.

Acknowledgements: The authors thank OMV E&P (OMV E&P GmbH, 2019) for providing access to the seismic data and granting permission to publish these findings. This work is financially supported by the Federal Ministry of Education and Research (BMBF) project "3G-GWD" with references 05A20GU5 and 05A23GU5 and partially funded by the European Union's Horizon 2020 research and innovation programme under the Marie Skłodowska-Curie grant agreement No. 955515 (SPIN ITN - https://spin-itn.eu). Special thanks goes to Conny Hammer and Alexander Bauer for their insightful comments on technical questions.

REFERENCES

Badrinarayanan, V., Kendall, A., Cipolla, R., 2017. SegNet: A Deep Convolutional Encoder-Decoder Architecture for Image Segmentation. IEEE Trans. Pattern Anal. Mach. Intell. 39, 2481–2495. https://doi.org/10.1109/TPAMI.2016.2644615

Bakhashwain, N., Sagheer, A., 2021. Online Tuning of Hyperparameters in Deep LSTM for Time Series Applications. Int. J. Intell. Eng. Syst. 14.

Barnes, A.E., 2007. A tutorial on complex seismic trace analysis. GEOPHYSICS 72, W33–W43. https://doi.org/10.1190/1.2785048

Bensen, G.D., Ritzwoller, M.H., Barmin, M.P., Levshin, A.L., Lin, F., Moschetti, M.P., Shapiro, N.M., Yang, Y., 2007. Processing seismic ambient noise data to obtain reliable broad-band surface wave dispersion measurements. Geophys. J. Int. 169, 1239–1260. https://doi.org/10.1111/j.1365-246X.2007.03374.x

Beveren, V. van, Bader, M., Brand, J. van den, Bulten, H.J., Campman, X., Koley, S., Linde, F., 2023. A study of deep neural networks for Newtonian noise subtraction at Terziet in Limburg—the Euregio Meuse-Rhine candidate site for Einstein Telescope. Class. Quantum Gravity 40, 205008. https://doi.org/10.1088/1361-6382/acf3c8

Castellanos, J.C., Clayton, R.W., Juarez, A., 2020. Using a Time-Based Subarray Method to Extract and Invert Noise-Derived Body Waves at Long Beach, California. J. Geophys. Res. Solid Earth 125, e2019JB018855. https://doi.org/10.1029/2019JB018855

Chandra, G., Yadav, S., Krishna, B.A., Kamaraju, M., 2014. Performance of wiener filter and adaptive filter for noise cancellation in real-time environment. Int. J. Comput. Appl. 97.

Chen, J., Benesty, J., Huang, Y., Doclo, S., 2006. New insights into the noise reduction Wiener filter. IEEE Trans. Audio Speech Lang. Process. 14, 1218–1234. https://doi.org/10.1109/TSA.2005.860851

Chollet, F., others, 2015. Keras [WWW Document]. URL https://github.com/fchollet/keras

Crameri, F., 2023. Scientific colour maps. https://doi.org/10.5281/zenodo.8409685

Du, S., Li, T., Yang, Y., Horng, S.-J., 2020. Multivariate time series forecasting via attention-based encoder–decoder framework. Neurocomputing 388, 269–279. https://doi.org/10.1016/j.neucom.2019.12.118

Harms, J., Naticchioni, L., Calloni, E., De Rosa, R., Ricci, F., D'Urso, D., 2022. A lower limit for Newtonian-noise models of the Einstein Telescope. Eur. Phys. J. Plus 137, 687. https://doi.org/10.1140/epjp/s13360-022-02851-z

Havskov, J., Alguacil, G., 2016. Correction for Instrument Response, in: Instrumentation in Earthquake Seismology. Springer International Publishing, Cham, pp. 197–230. https://doi.org/10.1007/978-3-319-21314-9_6

Helmy, T., Anifowose, F., Faisal, K., 2010. Hybrid computational models for the characterization of oil and gas reservoirs. Expert Syst. Appl. 37, 5353–5363. https://doi.org/10.1016/j.eswa.2010.01.021

Kawakami, H., Oyunchimeg, M., 2003. Normalized input–output minimization analysis of wave propagation in buildings. Eng. Struct. 25, 1429–1442. https://doi.org/10.1016/S0141-0296(03)00103-2

Kerber, F., Hurlebaus, S., Beadle, B.M., Stöbener, U., 2007. Control concepts for an active vibration isolation system. Mech. Syst. Signal Process. 21, 3042–3059. https://doi.org/10.1016/j.ymssp.2007.04.003

Kim, S.J., Dean, R., Flowers, G., Chen, C., 2009. Active Vibration Control and Isolation for Micromachined Devices. J. Mech. Des. 131. https://doi.org/10.1115/1.3159042

Knispel, S., Walda, J., Zehn, R., Bauer, A., Gajewski, D., 2022. A self-attention enhanced encoder-decoder network for seismic data denoising. Presented at the Second International Meeting for Applied Geoscience & Energy, Society of Exploration Geophysicists and American Association of Petroleum …, pp. 2922–2926.

LeCun, Y., Bengio, Y., Hinton, G., 2015. Deep learning. Nature 521, 436–444. https://doi.org/10.1038/nature14539

Li, D., Peng, S., Lu, Y., Guo, Y., Cui, X., 2019. Seismic structure interpretation based on machine learning: A case study in coal mining. Interpretation 7, 1–44. https://doi.org/10.1190/int-2018-0208.1

Li, W., Chakraborty, M., Fenner, D., Faber, J., Zhou, K., Rümpker, G., Stöcker, H., Srivastava, N., 2022. EPick: Attention-based multi-scale UNet for earthquake detection and seismic phase picking. Front. Earth Sci. 10. https://doi.org/10.3389/feart.2022.953007

Li, Z., Meier, M.-A., Hauksson, E., Zhan, Z., Andrews, J., 2018. Machine Learning Seismic Wave Discrimination: Application to Earthquake Early Warning. Geophys. Res. Lett. 45. https://doi.org/10.1029/2018GL077870

Lindsey, N.J., Rademacher, H., Ajo-Franklin, J.B., 2020. On the Broadband Instrument Response of Fiber-Optic DAS Arrays. J. Geophys. Res. Solid Earth 125, e2019JB018145. https://doi.org/10.1029/2019JB018145

M. Bath, 1973. Introduction to Seismology, Halsted Press book. Wiley.

M. Saad, O., Chen, Y., 2020. Deep Denoising Autoencoder for Seismic Random Noise Attenuation. Geophysics 85. https://doi.org/10.1190/geo2019-0468.1

Malhotra, P., Ramakrishnan, A., Anand, G., Vig, L., Agarwal, P., Shroff, G., 2016. LSTM-based Encoder-Decoder for Multi-sensor Anomaly Detection. CoRR abs/1607.00148.

Mousavi, S.M., Beroza, G.C., 2023. Machine Learning in Earthquake Seismology. Annu. Rev. Earth Planet. Sci. 51, 105–129. https://doi.org/10.1146/annurev-earth-071822-100323

Neuffer, T., Kremers, S., Fritschen, R., 2019. Characterization of seismic signals induced by the operation of wind turbines in North Rhine-Westphalia (NRW), Germany. J. Seismol. 23, 1161–1177. https://doi.org/10.1007/s10950-019-09866-7

OMV E&P GmbH, 2019. OMV.

Punturo, M., Abernathy, M., Acernese, F., Allen, B., Andersson, N., Arun, K., Barone, F., Barr, B., Barsuglia, M., Beker, M., Beveridge, N., Birindelli, S., Bose, S., Bosi, L., Braccini, S., Bradaschia, C., Bulik, T., Calloni, E., Cella, G., Mottin, E.C., Chelkowski, S., Chincarini, A., Clark, J., Coccia, E., Colacino, C., Colas, J., Cumming, A., Cunningham, L., Cuoco, E., Danilishin, S., Danzmann, K., Luca, G.D., Salvo, R.D., Dent, T., Rosa, R.D., Fiore, L.D., Virgilio, A.D., Doets, M., Fafone, V., Falferi, P., Flaminio, R., Franc, J., Frasconi, F., Freise, A., Fulda, P., Gair, J., Gemme, G., Gennai, A., Giazotto, A., Glampedakis, K., Granata, M., Grote, H., Guidi, G., Hammond, G., Hannam, M., Harms, J., Heinert, D., Hendry, M., Heng, I., Hennes, E., Hild, S., Hough, J., Husa, S., Huttner, S., Jones, G., Khalili, F., Kokeyama, K., Kokkotas, K., Krishnan, B., Lorenzini, M., Lück, H., Majorana, E., Mandel, I., Mandic, V., Martin, I., Michel, C., Minenkov, Y., Morgado, N., Mosca, S., Mours, B., Müller–Ebhardt, H., Murray, P., Nawrodt, R., Nelson, J., Oshaughnessy, R., Ott, C.D., Palomba, C., Paoli, A., Parguez, G., Pasqualetti, A., Passaquieti, R., Passuello, D., Pinard, L., Poggiani, R., Popolizio, P., Prato, M., Puppo, P., Rabeling, D., Rapagnani, P., Read, J., Regimbau, T., Rehbein, H., Reid, S., Rezzolla, L., Ricci, F., Richard, F., Rocchi, A., Rowan, S., Rüdiger, A., Sassolas, B., Sathyaprakash, B., Schnabel, R., Schwarz, C., Seidel, P., Sintes, A., Somiya, K., Speirits, F., Strain, K., Strigin, S., Sutton, P., Tarabrin, S., Thüring, A., Brand, J. van den, Leewen, C. van, Veggel, M. van, Broeck, C. van den, Vecchio, A., Veitch, J., Vetrano, F., Vicere, A., Vyatchanin, S., Willke, B., Woan, G., Wolfango, P., Yamamoto, K., 2010. The Einstein Telescope: a third-generation gravitational wave observatory. Class. Quantum Gravity 27, 194002. https://doi.org/10.1088/0264-9381/27/19/194002

Ronneberger, O., Fischer, P., Brox, T., 2015. U-net: Convolutional networks for biomedical image segmentation, in: Medical Image Computing and Computer-Assisted Intervention–MICCAI 2015: 18th International Conference, Munich, Germany, October 5-9, 2015, Proceedings, Part III 18. Springer, pp. 234–241.

Rost, S., Thomas, C., 2002. ARRAY SEISMOLOGY: METHODS AND APPLICATIONS. Rev. Geophys. 40, 2–1. https://doi.org/10.1029/2000RG000100

Sabra, K.G., Gerstoft, P., Roux, P., Kuperman, W.A., Fehler, M.C., 2005. Extracting time-domain Green's function estimates from ambient seismic noise. Geophys. Res. Lett. 32. https://doi.org/10.1029/2004GL021862

Schaff, D.P., Bokelmann, G.H.R., Beroza, G.C., Waldhauser, F., Ellsworth, W.L., 2002. High-resolution image of Calaveras Fault seismicity. J. Geophys. Res. Solid Earth 107, ESE 5-1-ESE 5-16. https://doi.org/10.1029/2001JB000633

Schippkus, S., Garden, M., Bokelmann, G., 2020. Characteristics of the Ambient Seismic Field on a Large-N Seismic Array in the Vienna Basin. Seismol. Res. Lett. 91, 2803–2816. https://doi.org/10.1785/0220200153

Schippkus, S., Snieder, R., Hadziioannou, C., 2022. Seismic interferometry in the presence of an isolated noise source. Seismica 1. https://doi.org/10.26443/seismica.v1i1.195

Sergeant, A., Chmiel, M., Lindner, F., Walter, F., Roux, P., Chaput, J., Gimbert, F., Mordret, A., 2020. On the Green's function emergence from interferometry of seismic wave fields generated in high-melt glaciers: implications for passive imaging and monitoring. The Cryosphere 14, 1139–1171. https://doi.org/10.5194/tc-14-1139-2020

Snieder, R., 2004. Extracting the Green's function from the correlation of coda waves: A derivation based on stationary phase. Phys Rev E 69, 046610. https://doi.org/10.1103/PhysRevE.69.046610

Tariq, Z., Aljawad, M., Hassan, A., Murtaza, M., Mohammed, E., El Husseiny, A., Alarifi, S., Abdulraheem, A., 2021. A systematic review of data science and machine learning applications to the oil and gas industry. J. Pet. Explor. Prod. Technol. 11. https://doi.org/10.1007/s13202-021-01302-2

Tol, Paul, 2021. "Colour Schemes." Technical note SRON/EPS/TN/09-002 3.2. SRON. URL https://personal.sron.nl/~pault/data/colourschemes.pdf.

Verma, N., Maurya, S.P., kant, R., Singh, K.H., Singh, Raghav, Singh, A.P., Hema, G., Srivastava, M.K., Tiwari, A.K., Kushwaha, P.K., Singh, Richa, 2024. Comparison of neural networks techniques to predict subsurface parameters based on seismic inversion: a machine learning approach. Earth Sci. Inform. 17, 1031–1052. https://doi.org/10.1007/s12145-023-01199-x

Walden, A.T., White, R.E., 1998. Seismic wavelet estimation: a frequency domain solution to a geophysical noisy input-output problem. IEEE Trans. Geosci. Remote Sens. 36, 287–297. https://doi.org/10.1109/36.655337

Weerts, H.J.P., Mueller, A.C., Vanschoren, J., 2020. Importance of Tuning Hyperparameters of Machine Learning Algorithms arXiv preprint arXiv:2007.07588. https://doi.org/10.48550/arXiv.2007.07588

Wegler, U., Sens-Schönfelder, C., 2007. Fault zone monitoring with passive image interferometry. Geophys. J. Int. 168, 1029–1033. https://doi.org/10.1111/j.1365-246X.2006.03284.x

Wu, H., Zhang, B., Lin, T., Cao, D., Lou, Y., 2019. Semiautomated seismic horizon interpretation using the encoder-decoder convolutional neural network. Geophysics 84, B403–B417.

Wu, Y., Wang, W., Zhu, G., Wang, P., 2021. Application of seismic multiattribute machine learning to determine coal strata thickness. J. Geophys. Eng. 18, 834–844. https://doi.org/10.1093/jge/gxab054

Xie, Y., Ebad Sichani, M., Padgett, J., Desroches, R., 2020. The promise of implementing machine learning in earthquake engineering: A state-of-the-art review. Earthq. Spectra 36, 875529302091941. https://doi.org/10.1177/8755293020919419

Yang, L., Shami, A., 2020. On hyperparameter optimization of machine learning algorithms: Theory and practice. Neurocomputing 415, 295–316. https://doi.org/10.1016/j.neucom.2020.07.061

Yin, J., Denolle, M.A., He, B., 2022. A multitask encoder–decoder to separate earthquake and ambient noise signal in seismograms. Geophys. J. Int. 231, 1806–1822. https://doi.org/10.1093/gji/ggac290

Zhang, H., Chen, T., Liu, Y., Zhang, Y., Liu, J., 2021. Automatic seismic facies interpretation using supervised deep learning. GEOPHYSICS 86, IM15–IM33. https://doi.org/10.1190/geo2019-0425.1

Zhong, T., Cheng, M., Dong, X., Li, Y., Wu, N., 2022. Seismic random noise suppression by using deep residual U-Net. J. Pet. Sci. Eng. 209, 109901. https://doi.org/10.1016/j.petrol.2021.109901

Zhu, W., Beroza, G.C., 2019. PhaseNet: a deep-neural-network-based seismic arrival-time picking method. Geophys. J. Int. 216, 261–273. https://doi.org/10.1093/gji/ggy423